Investigation on Amino-Induced *In-Situ* Interfacial Copolymerization Nanofiltration Membranes for Dye-Containing Wastewater Separation

Si Zhang[1,2], Hao Zhang[1,*], Zhenjie Gu[1,3,*] and Zhihua Qiao[1,2]

[1]*State Key Laboratory of Advanced Separation Membrane Materials, Tiangong University, Tianjin 300387, China*

[2]*School of Chemistry and Chemical Engineering, Tiangong University, Tianjin 300387, China*

[3]*School of Physical Science and Technology, Tiangong University, Tianjin 300387, China*

Abstract: To address the demand for efficient dye separation and salt recovery in textile wastewater treatment, this study proposes a fabrication strategy for composite nanofiltration (NF) membranes modified with UiO-66-NH_2. This approach involves introducing varying proportions of UiO-66-NH_2 into the aqueous phase solution during interfacial polymerization. By leveraging the abundant amino active sites on the UiO-66-NH_2 to undergo covalent reactions with acyl chloride monomers in the organic phase, *in-situ* chemical bonding between the MOF material and the polyamide (PA) separation layer was achieved concurrently with the interfacial polymerization of piperazine (PIP) and trimesoyl chloride (TMC). This method significantly enhanced the interfacial compatibility between the MOF nanoparticles and the polymer matrix, successfully yielding a series of thin-film nanocomposite (TFN) membranes with robust interfacial bonding characteristics. The incorporation of UiO-66-NH_2 markedly improved membrane permeability and optimized its rejection performance toward various dyes. At an optimal loading of 0.15 wt%, the pure water flux of the composite membrane reached 45.77 $L \cdot m^{-2} \cdot h^{-1}$, representing an increase of more than 80% compared with the pristine membrane (24.65 $L \cdot m^{-2} \cdot h^{-1}$). Meanwhile, rejection efficiencies for methyl blue (MeB) and congo red (CR) were as high as 98.0%, while methyl orange (MO) and methylene blue (MB) achieved rejections exceeding 75.0% (75.6% and 83%, respectively). The membrane also exhibited good operational stability during a 12 h continuous filtration test, maintaining a flux decline of less than 8.5% and dye rejection rates stably maintained above 98% (for CR) and 75% (for MO), respectively. UiO-66-NH_2 was uniformly incorporated into the PA network and formed stable covalent bonds, which effectively regulated the physicochemical properties of the membrane surface and separation channels, thereby simultaneously enhancing the water flux and dye rejection efficiency. This study provided an effective approach for developing NF membranes with high water permeability, high retention rate, and good stability for dye wastewater treatment.

Keywords: Textile wastewater, Nanofiltration membrane, Metal-organic framework, UiO-66-NH_2, Interfacial polymerization, Dye rejection.

1. INTRODUCTION

The textile dyeing and printing industry, as a vital pillar industry, was accompanied by severe pollution from dyeing wastewater due to its rapid development [1]. The textile dyeing wastewater was characterized by a complex composition containing large amounts of recalcitrant organic dyes and inorganic salts, along with high chromaticity and high chemical oxygen demand (COD). Direct discharge of such wastewater posed serious threats to aquatic ecosystems and human health [2].

To address the challenges of water pollution and water scarcity, the development of efficient, energy-saving, and environmentally friendly wastewater treatment technologies was urgently required. Chemical methods (*e.g.*, advanced oxidation processes) were limited by high costs and were prone to cause secondary pollution, while biological methods were sensitive to water quality, required long treatment periods, and exhibited limited removal efficiency for certain dyes [3]. In contrast, membrane separation was recognized for its advantages, including high efficiency, energy savings, operational simplicity, and environmental friendliness, and demonstrated broad application prospects in the treatment of dye wastewater [4]. Nanofiltration (NF) was defined as a pressure-driven membrane technology positioned between ultrafiltration and reverse osmosis with a pore size of approximately 1 nm. By leveraging the size-sieving effect and the Donnan electrostatic exclusion effect, dye molecules (200–1000 Da) and multivalent salt ions could be efficiently retained, while partial permeation of monovalent salts was allowed. This characteristic enabled selective separation of dyes and salts in the treatment of dyeing wastewater. The process was characterized by high efficiency, low energy consumption, and phase change-free operation—attributes that position NF as a key technology for the green treatment and resource recovery of wastewater.

*Address correspondence to this author at the State Key Laboratory of Advanced Separation Membrane Materials, Tiangong University, Tianjin 300387; Tel: +86-138-0593-3826; +86-181-0206-3306;
E-mail: fgzhanghao@tiangong.edu.cn; guzhenjie@tiangong.edu.cn

Received on 03-03-2026 Accepted on 01-04-2026 Published on 02-04-2026

E-ISSN: 2311-8717/26

Currently, the thin-film composite (TFC) membrane is the primary membrane structure for the NF process. It typically consists of three layers: a bottom non-woven fabric that provided mechanical support; a middle ultrafiltration membrane prepared on the non-woven substrate via phase inversion, and a top polyamide (PA) selective separation layer, with a thickness ranging from tens to hundreds of nanometers, formed by interfacial polymerization [5]. The structure of the PA layer directly determined the separation performance of the membrane, making the precise control of its microscopic structure crucial. Interfacial polymerization was established as a primary method for preparing high-performance NF membranes. In this process, amine monomers from the aqueous phase and acyl chloride monomers from the organic phase were reacted on the surface of a ultrafiltration membrane, through which a dense PA selective layer was formed [6]. The method has significant advantages of rapid reaction rate, uniform membrane formation, and controllable structure. To further enhance the separation performance and stability of NF membranes, functional nanomaterials such as titanium dioxide (TiO_2) [7], graphene oxide (GO) [8], and MOFs were frequently introduced into the interfacial polymerization process to tailor the microscopic structure and surface properties of the separation layer.

MOFs are particularly recognized for their high specific surface area, adjustable pore sizes, and abundant surface functional groups, making them promising candidates for dye/salt separation in textile wastewater treatment [9-11]. Their tunable porous structures, chemical stability, and functionalization potential have driven significant progress in the fabrication and performance optimization of MOF-based thin-film nanocomposite (TFN) membranes. However, current mainstream preparation strategies — including physical blending and *in-situ* growth—still suffer from inherent limitations that hinder practical application.

Physical blending is a widely used method for fabricating MOF-TFN membranes, involving direct dispersion of MOF nanoparticles into the aqueous or organic phase during interfacial polymerization. For example, Aljundi *et al*. [9] incorporated 0.4 wt% ZIF-8 into the PA layer, significantly enhancing membrane surface hydrophilicity. It weakened hydrophobic interactions with organic pollutants, endowing the membrane with high permeability and a 75% reduction in bovine serum albumin (BSA) induced fouling. However, the thin PA layer formed via conventional interfacial polymerization struggles to effectively encapsulate and tightly embed MOF nanoparticles, easily causing interfacial defects. Similarly, Li *et al*. [10] incorporated MIL-53(Fe) into the PA layer via physical blending, achieving enhanced water flux and high dye rejection. But the lack of chemical bonding caused MOF agglomeration, Fe^{2+}/Fe^{3+} leaching, and PA layer degradation. The issues are intrinsic to physical blending, as weak interfacial interactions fail to resolve MOF dispersion, particle leaching, and structural compatibility with the PA matrix.

In-situ growth strategies aim to improve MOF dispersion and interfacial adhesion by growing MOF particles directly on the support or within the PA layer. Wu *et al*. [11] fabricated ZIF-8-TFN membranes via two-step *in-situ* growth (ZIF-8 first grown on PSf support before IP), achieving a water flux of 20.8 $L \cdot m^{-2} \cdot h^{-1} \cdot bar^{-1}$ and ultrahigh anionic dye rejection. But the process required rigorous reaction condition control and was complex and time-consuming. Similarly, Wu *et al*. [12] prepared MOF-808 membranes via *in-situ* solvothermal growth on PVP-modified α-Al_2O_3 tubes, which exhibited excellent dye rejection and long-term stability, yet suffered from low water flux. The solvothermal growth demanded 48 h at 140℃ and PVP modification for heterogeneous nucleation increased preparation complexity and scalability challenges. Common drawbacks of *in-situ* growth include strict process control, prolonged fabrication cycles, and difficulty in uniform MOF distribution throughout the entire PA layer, restricting further performance optimization.

UiO-66-NH_2, as an amino-functionalized MOF, was noted not only for its favorable hydrothermal and chemical stability, but also for the ability of its surface amino groups to interact with the PA layer, thereby enhancing the interfacial adhesion while simultaneously improving the hydrophilicity and separation selectivity of the membrane [13]. To address these critical gaps, we propose an amino-induced *in-situ* copolymerization strategy — a distinct approach that differs fundamentally from physical blending and *in-situ* growth. By incorporating UiO-66-NH_2 as an active modifier into the interfacial polycondensation system, the amino groups on UiO-66-NH_2 participate in the polymerization reaction, forming covalent bonds with the PA matrix. This unique mechanism achieves two key advantages that address the limitations of existing strategies: (1) stable chemical bonding between MOF and PA, preventing particle leaching and enhancing long-term operational stability; (2) simplified preparation process with mild reaction conditions, avoiding the strict control requirements of *in-situ* growth and the interfacial defects of physical blending.

By systematically adjusting the doping ratio of UiO-66-NH_2, a series of composite NF membranes with

enhanced interfacial compatibility, superior permeability, and high selective separation performance were fabricated. To comprehensively evaluate their separation performance, four typical anionic and cationic dyes—methyl blue (MeB), congo red (CR), methyl orange (MO), and methylene blue (MB)—were employed as model contaminants. The rejection behavior and flux evolution of the composite membranes toward dyes with varying charge properties and molecular weights were systematically investigated.

2. RESULTS AND DICUSSION

The TFN membranes were fabricated via the procedure illustrated in Figure **1**, the mechanism of which will be elaborated in the membrane synthesis section.

2.1. Characterization of Filler

The FTIR spectra of UiO-66 and UiO-66-NH_2 crystals are shown in Figure **2**(**a**). Compared with UiO-66, stretching vibration peaks attributable to the C-N bond were observed at 1260 cm^{-1} and 1337 cm^{-1} for UiO-66-NH_2, a bending vibration peak of the N-H bond was detected at 1700 cm^{-1}, and notably, a distinct characteristic peak corresponding to the N-H stretching vibration was exhibited around 3400 cm^{-1}. The appearance of these characteristic peaks confirms that amino groups have been successfully incorporated into the UiO-66 framework [14]. These amino groups act as key reactive sites for the amino-induced *in-situ* copolymerization with the PA matrix. It forms the fundamental basis for the stable combination of UiO-66-NH_2 and the PA selective layer. It further ensures the structural integrity of the prepared TFN membranes.

The crystal structure of the synthesized UiO-66-NH_2 powder was characterized by XRD. As shown in Figure **2**(**b**), the measured XRD pattern exhibited a high degree of correspondence with the simulated pattern. Characteristic diffraction peaks of the UiO-66 series were observed at 2θ = 7.4°, 8.5°, and 25.7°, corresponding to the (1 1 1), (0 0 2), and (0 0 6) crystal planes, respectively [15]. No noticeable impurity peaks were observed in the pattern, which confirms that the target MOF was successfully synthesized.

Figure **2**(**c**) presents the N_2 adsorption-desorption isotherm and the corresponding pore size distribution of UiO-66-NH_2. The BET surface area of the UiO-66-NH_2 was determined to be 918.0 m^2/g. Meanwhile, pore size analysis using the H-K method revealed that the pore sizes were predominantly centered around 0.6 nm. The high BET surface area provides abundant active sites for the *in-situ* copolymerization reaction with the PA matrix, promoting the uniform dispersion of UiO-66-NH_2 in the PA layer. The narrow pore size distribution centered at ~0.6 nm is smaller than the majority of dye molecules but is larger than the kinetic diameter of water (~0.28 nm). It allows UiO-66-NH_2 to form fast transport channels for water and a physical barrier for dyes, laying a structural basis for improved water flux and dye rejection in TFN membranes. The highly developed porous structure of UiO-66-NH_2 is demonstrated to provide a favourable basis for the subsequent fabrication of TFC membranes.

Figure **2**(**d**) shows the SEM image of UiO-66-NH_2, whose crystal morphology is almost identical to that of UiO-66 (Figure **S1**). The sample was observed to consist of octahedron, regularly polyhedral crystalline particles with a uniform size distribution and good dispersion. The particle surfaces were characterized as

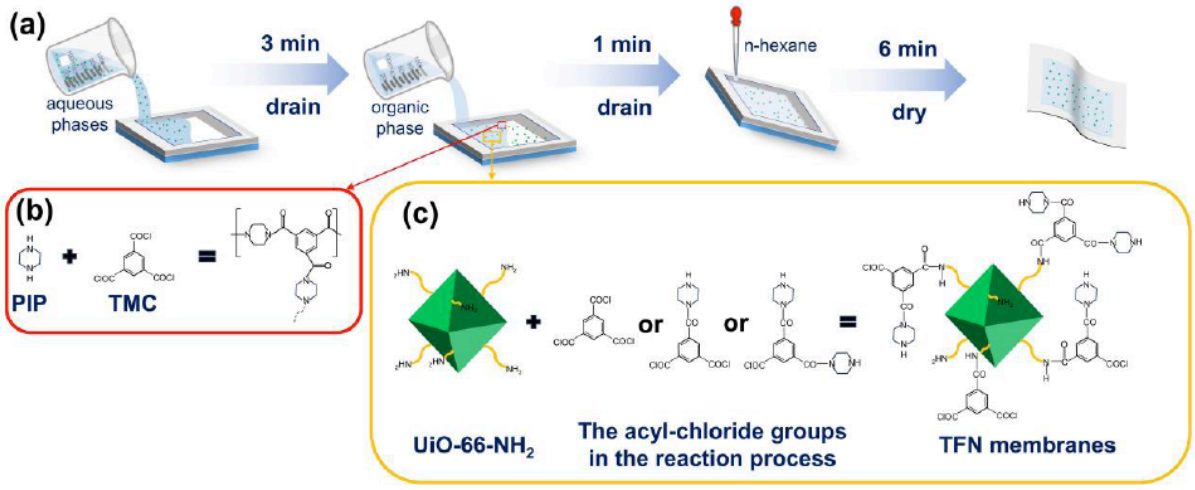

Figure 1: Schematic of the TFN membranes preparation: (**a**) the flowchart for the preparation of TFN membranes; (**b**) mechanism of traditional interfacial polymerization; (**c**) mechanism diagram for interfacial polymerization involving UiO-66-NH_2.

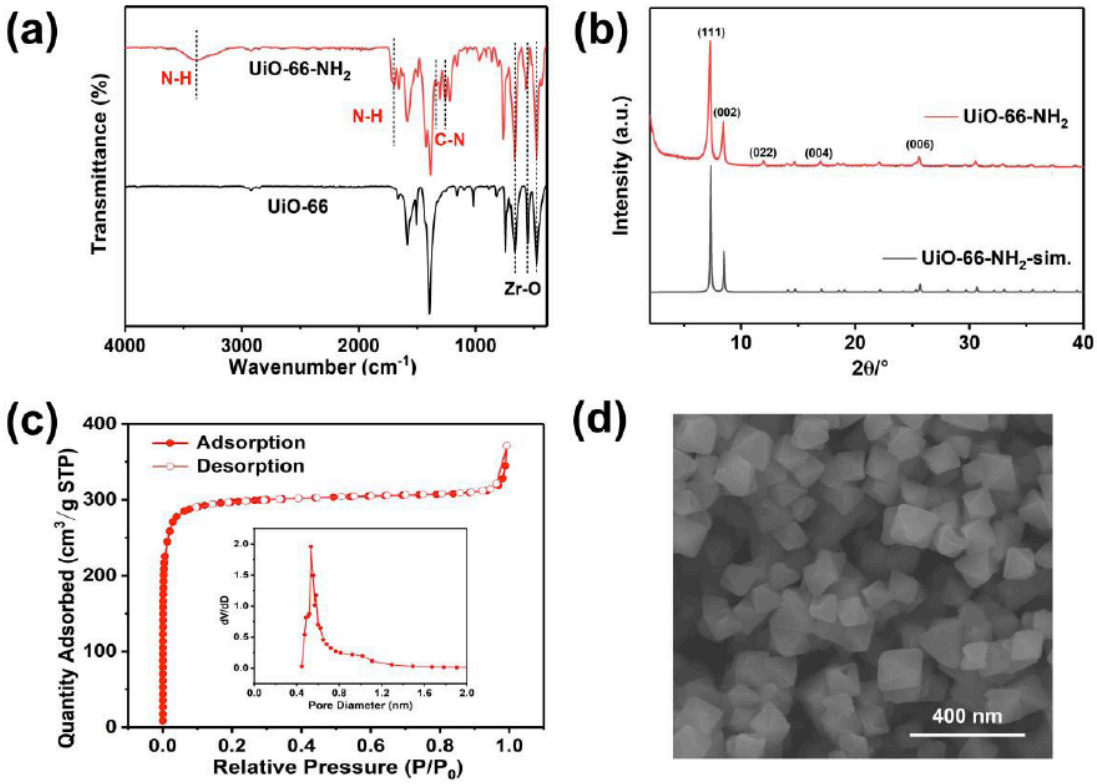

Figure 2: (**a**) FTIR spectra of UiO-66 and UiO-66-NH_2; (**b**) the XRD patterns of UiO-66-NH_2; (**c**) N_2 adsorption-desorption isotherms of UiO-66-NH_2; (**d**) SEM image of UiO-66-NH_2.

smooth with clear edges and corners, indicating sufficient crystal growth and a structurally intact framework.

2.2. Fabrication of the TFN Membrane

The fabrication of the TFN membrane was schematically illustrated in Figure **1**. The formation of the TFN membrane was based on the classical interfacial polymerization reaction. With the participation of the UiO-66-NH_2, amino-induced *in-situ* interfacial copolymerization nanofiltration membranes are ultimately formed. As shown in Figure **1**(**b**), the PIP monomer from the aqueous phase was transported to the liquid-liquid interface, where a rapid acyl chloride-amine condensation reaction was initiated with TMC from the organic phase, resulting in the formation of a cross-linked PA thin membrane [16]. Figure **1**(**c**) indicated that when UiO-66-NH_2 was present in the aqueous phase, the abundant amino groups (-NH_2) on its surface served as additional active sites and were also able to react with TMC. Consequently, the MOF were chemically anchored via covalent bonding within the growing PA network, rather than being merely physically doped [17].

The introduction of UiO-66-NH_2 enabled effective regulation and optimization of the PA selective layer formation. The MOF served as heterogeneous nucleation sites, guiding the more ordered deposition of PA. Their surface reaction locally consumed TMC, which moderately modulated the interfacial polymerization rate and favoured the formation of a more uniform separation layer [18]. Meanwhile, the well-defined micropores (approximately 0.6 nm) inherent to the MOF, together with the interfaces created between the MOF and the polymer matrix, functioned as rapid transport channels for water molecules, significantly reducing the mass transfer resistance of water. The rigid framework of the MOF particles also suppressed the relaxation and swelling of the PA chains, thereby enhancing the stability of the membrane [19]. The presence of amino groups on the UiO-66-NH_2 surface substantially altered the surface chemistry of the PA layer. At an addition level of 0.15 wt%, the MOF particles were uniformly distributed on the membrane surface. However, when the addition exceeded 0.2 wt%, particle agglomeration and prominent protrusions were observed, which affected the Zeta potential and hydrophilicity of the membrane. As a result, the separation selectivity based on the synergistic effects of size sieving and the Donnan effect was cooperatively tuned. These aspects were discussed in detail in the section on membrane characterization and analysis.

2.3. Characterization of the TFN Membrane

UiO-66-NH_2 was introduced into the aqueous phase, and the TFN membrane was prepared via an

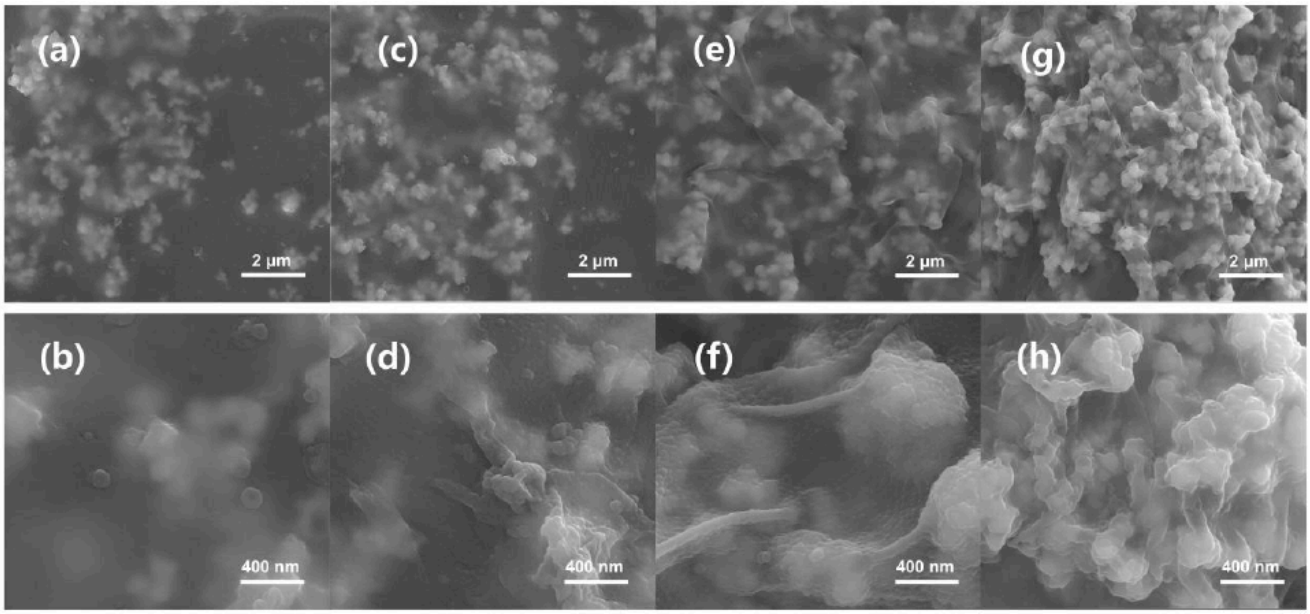

Figure 3: SEM images of TFN membranes with different UiO-66-NH_2 loadings: (**a**), (**b**) TFN-0.05 membrane; (**c**), (**d**) TFN-0.1 membrane; (**e**), (**f**) TFN-0.15 membrane; (**g**), (**h**)TFN-0.2 membrane.

amino-induced *in-situ* copolymerization strategy. The surface morphology of the TFN membranes were characterized by SEM, as shown in Figure **3**. Compared with the relatively smooth surface of the TFN-0 membrane (Figure **S2**), significant changes in the surface morphology were observed upon the incorporation of UiO-66-NH_2. As shown in Figure **3**(**a**) and **3**(**b**), at loadings ≤ 0.15 wt%, the surface of the TFN membranes was uniformly covered with a large number of UiO-66-NH_2. Specifically, at the 0.15 wt% loading, the surface protrusions were distributed most uniformly and densely, and were well-integrated with the PA matrix. At this optimal loading, UiO-66-NH_2 exhibited the best dispersibility and was effectively embedded into the PA network. It optimized the pore size distribution of the PA selective layer and formed a dense, uniform microporous structure with suitable effective pore size. It provides a structural basis for the enhanced size sieving effect in dye separation. Additionally, UiO-66-NH_2 acted as a heterogeneous nucleation site to optimize the interfacial polymerization process.

However, with a further increase in UiO-66-NH_2 loading to 0.2 wt%, the membrane surface morphology exhibited obvious deterioration. The agglomeration of MOF particles leads to significant unevenly distributed protrusions on the membrane surface, which seriously affects the surface uniformity of the membrane. In Figure **3**(**d**), severe agglomeration and stacking of UiO-66-NH_2 particles could be clearly observed. These agglomerates were embedded within the PA matrix, forming a rough 'peak-and-valley' structure. The morphology indicated that the excessive MOF particles agglomerated due to decreased dispersibility, which disrupted the homogeneity of the interfacial polymerization reaction. The structural disorder not only destroyed the uniformity of the effective pore size but also increased the non-selective transport channels, thus weakening the size sieving performance of the membrane. Consequently, the PA layer disordered in order to encapsulate these agglomerates, thereby increasing the mass transfer resistance. Based on this, TFN-U membrane was prepared with UiO-66 at the same loading (0.15 wt%). But its SEM image (Figure **S3**) shows obvious defects on the membrane surface. The defects arise from the lack of reactive amino groups on UiO-66, resulting in poor interfacial compatibility. The defects create large non-selective channels of the TFN-U membrane. SEM analysis directly demonstrated that the MOF loading decisively affected both the dispersion state of the particles and the structure of the resulting membrane layer, and thus dominated the size sieving effect of the TFN-0.15 membranes in dye separation processes.

In contrast to the TFN-0 membrane, the TFN-0.15 membrane exhibited a distinct Zr 3d peak in Figure **4**(**a**), providing evidence for the presence of UiO-66-NH_2 on its surface. In Figure **4**(**b**) and (**c**), the distinct peak shifts in the N 1s and O 1s XPS spectra further confirm the formation of covalent bonds between UiO-66-NH_2 and the PA matrix via *in-situ* copolymerization strategy [17]. The interfacial compatibility of the membrane was thereby improved.

The elemental composition on the surface of the TFN-0.15 membrane was analyzed using EDS. As

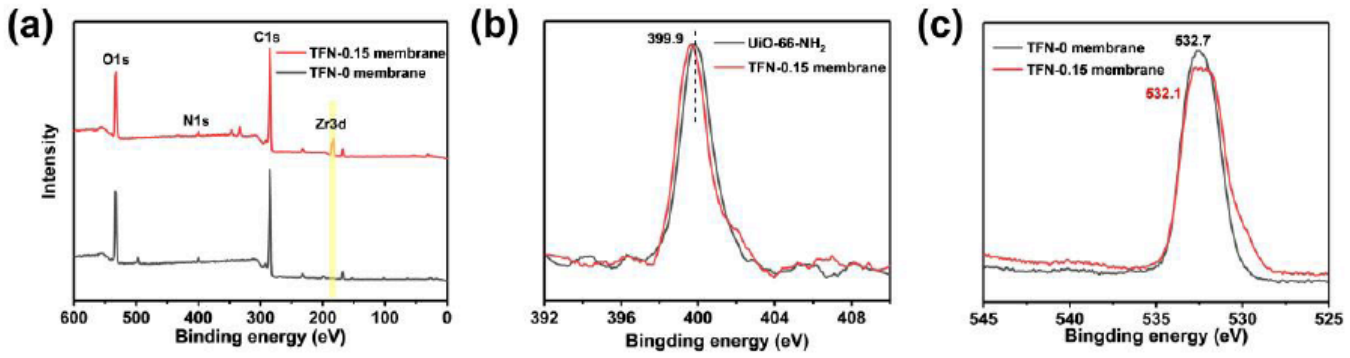

Figure 4: XPS spectra: (**a**) full spectrum; (**b**) N 1s; (c) O 1s.

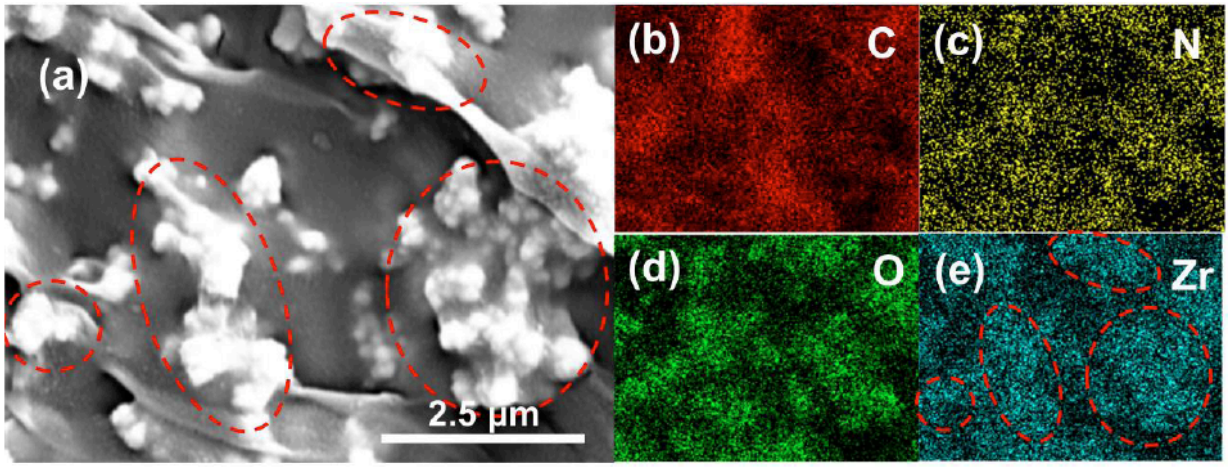

Figure 5: SEM-EDS of images for TFN-0.15 membrane: (**a**) SEM image; (**b**) C; (**c**) N; (d) O; (e) Zr.

shown in Figure **5**, the uniform distributions of the C, N, and O elements indicated that a complete and homogeneous separation layer was formed via interfacial *in-situ* copolymerization. More critically, the uniform distribution of Zr, which serves as the characteristic element of the metal nodes in UiO-66-NH_2, directly confirmed that the MOF particles achieved a highly uniform dispersion within the PA matrix. The uniform distribution of UiO-66-NH_2 is a prerequisite for the formation of a homogeneous PA selective layer with consistent separation performance across the entire membrane surface. The strong spatial overlap of the elemental maps further demonstrated that a tightly integrated composite structure was formed between the MOF particles and the PA network. These results indicated that the UiO-66-NH_2 were effectively and uniformly embedded into the PA selective layer at the optimal loading of 0.15 wt%.

The zeta potential of TFN membranes with various UiO-66-NH_2 loadings as a function of pH is presented in Figure **6**(**a**). At pH < 3, the TFN membrane surfaces exhibited a positive charge. With increasing pH, the charges on the membrane surfaces all changed to negative charges. The hydrolysis of unreacted acyl chloride groups in TMC results in negatively charged TFN membranes at pH = 7. Elevating the UiO-66-NH_2 content from 0 wt% to 0.2 wt% led to a substantial rise in the zeta potential of the TFN membranes when measured at a fixed pH. This indicated that the introduction of amino groups from UiO-66-NH_2 weakened the negative charge and relatively enhanced the positive charge on the TFN membrane surface.The water contact angle of the membranes also exhibited a regular variation with the UiO-66-NH_2 loading, as shown in Figure **6**(**b**). With the increase of the addition amount of UiO-66-NH_2, the contact angle of the TFN membrane gradually decreased. This was attributed to the introduction of hydrophilic amino groups by the uniformly dispersed MOF. Meanwhile, SEM showed that uniform protrusions were formed on its surface, increasing the contact area between the membrane surface and water. It indicated that the incorporation of UiO-66-NH_2 is beneficial to improving the hydrophilicity of the membranes. The above results demonstrated that the MOF loading cooperatively governed the electrical and hydrophilic properties of the membranes by modulating their surface chemical composition and microscopic structure.

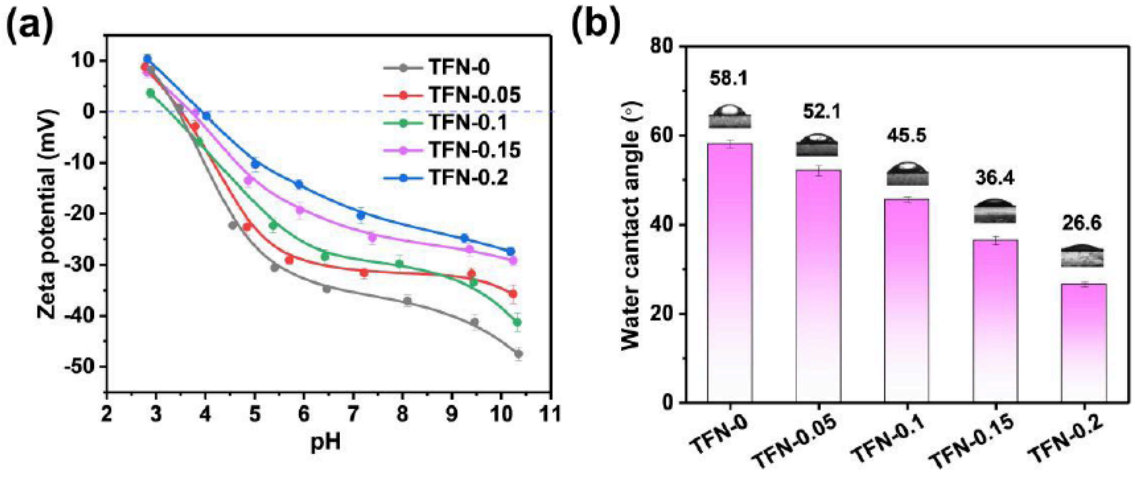

Figure 6: (**a**) Zeta potential test of TFN membrane surface; (**b**) Water contact angle test on membrane surface.

2.4. Analysis of Dye Separation Performance of TFN Membranes

Figure **7** systematically compared the permeability and separation performance of various TFN membranes at 5 bar. All the water flux and dye rejection rate presented in Figure **7** were obtained from three independent parallel experiments. Figure **7**(**a**) presentd the water fluxes of the five membranes for pure water and four dye solutions. The flux of all membranes toward dye solutions was slightly lower than their pure water flux, which was mainly caused by concentration polarization and membrane fouling, while the variation trend was generally consistent with that of pure water flux. Specifically, the pure water flux of the membranes first increased and then decreased with the increase of the addition amount of UiO-66-NH_2. The TFN-0.15 membrane achieved the maximum pure water flux of 45.77 $L \cdot m^{-2} \cdot h^{-1}$. Compared with the TFN-0 membrane, the enhanced water flux of other TFN membranes can be attributed to two factors. On the one hand, the improved surface roughness and hydrophilicity provided a larger effective area for water molecule transport. On the other hand, UiO-66-NH_2 possessed a pore size of approximately 0.6 nm, which offered low-resistance pathways for water molecules with a diameter of about 0.28 nm. When the UiO-66-NH_2 loading was further increased to 0.2 wt%, the flux decreased to 42.23 $L \cdot m^{-2} \cdot h^{-1}$. The above results indicate that an appropriate amount of MOF can optimize the structure of the PA selective layer and construct efficient water transport channels [20]. However, excessive MOF addition led to particle aggregation, resulting in structural disorder and local thickening of the PA layer, which significantly increased mass transfer resistance and thus markedly reduced the water flux of the membranes [21].

Figure **7**(**b**) revealed the different evolution patterns of the rejection rates for the four dyes with increasing UiO-66-NH_2 loading. Table **S1** summarizes a comprehensive performance comparison of our TFN membranes with five previously reported membranes for water flux and dye rejection. The results demonstrate that the TFN-0.15 membrane prepared in this work achieves a better balance between water flux and dye rejection. For the anionic macromolecular dyes MeB and CR, the TFN membrane exhibited rejection rates exceeding 95%. On the one hand, the optimized micro-pore structure of the PA layer induced

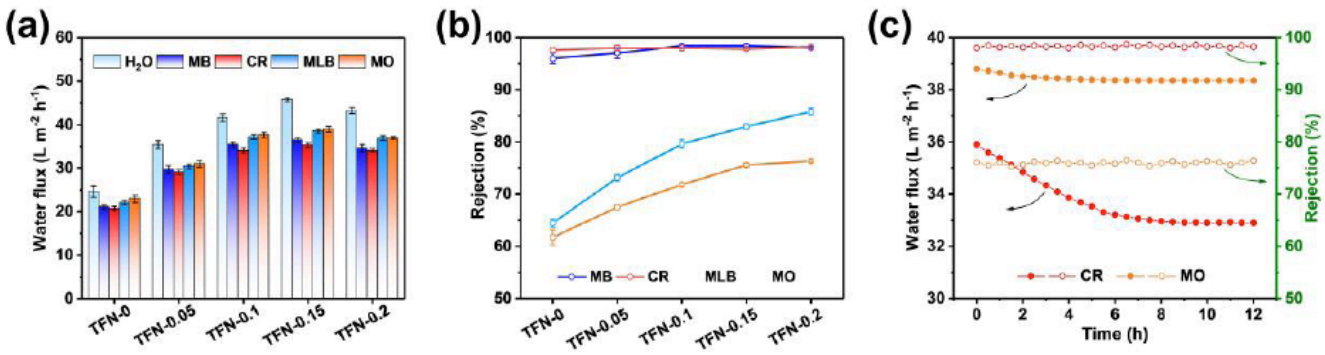

Figure 7: (**a**) Water flux of five membranes for pure water and four dyes; (**b**) rejection rates of 5 membranes against different dyes; (**c**) stability test of TFN-0.15 membrane for separation performance of CR and MO. Test conditions are the same, with dye concentrations of 0.1 g/L and a pressure of 0.5 MPa.

by uniformly dispersed UiO-66-NH_2 forms a strong physical barrier for macromolecular MeB and CR via size sieving, as their kinetic diameters are much larger than the effective pore size of the membrane. On the other hand, despite a temporary decrease in negative surface charge, the TFN-0.15 membrane still maintained effective electrostatic repulsion toward macromolecules. The synergistic effect ensures the efficient retention of macromolecular anionic dyes.

The membranes exhibited similar but slightly different rejection behaviors for small molecule dyes. Among TFN membranes, the rejection rate of the cationic dye MB increased continuously. This change is mainly attributed to the reduction of unfavorable electrostatic attraction between the membrane surface and cationic dyes, enabled by the incorporation of UiO-66-NH_2. Meanwhile, it provided additional adsorption sites and a more tortuous mass transfer pathway for dye molecules. Consequently, the rejection rate was effectively enhanced. With rising UiO-66-NH_2 incorporation, the TFN membranes showed a progressive improvement in MO rejection that subsequently plateaued. When the UiO-66-NH_2 loading was raised from 0 wt% to 0.2 wt%, the MO rejection rate achieved by the TFN membranes was elevated from 61.70% to 76.33%. Although the negative charge on the membrane surface decreased with increasing MOF loading, the rejection rate still increased. It indicated that the size sieving effect played a dominant role in the separation of small molecular anionic MO, and the Donnan effect had a negligible auxiliary effect due to the weakened membrane negative charge. UiO-66-NH_2 played a crucial role in modulating the PA layer's architecture, creating a more tortuous path that hindered the passage of MO molecules and consequently boosted the separation efficiency.

In summary, incorporating 0.15 wt% UiO-66-NH_2 enabled the membrane to simultaneously achieve high permeability and effective dye rejection, representing an optimal performance balance. The long-term stability test presented in Figure **7**(**c**) further demonstrated that during a 12 h continuous separation of CR and MO, both the water flux and rejection rates of the TFN-0.15 membrane remained stable with minimal fluctuations (CR rejection >98%, MO rejection >75%). These results confirmed that the amino-induced *in-situ* copolymerization strategy is viable, achieving the goal of both high flux and high retention rate of the membrane, and demonstrating its reliability and durability in practical applications.

3. CONCLUSION

In this study, an amino-induced *in-situ* interfacial copolymerization strategy was proposed, where UiO-66-NH_2 was introduced during the interfacial polymerization process to achieve *in-situ* chemical bonding between the MOF material and the PA separation layer. The results demonstrated that an appropriate amount of UiO-66-NH_2 was uniformly embedded into the PA network through a covalent bonding mechanism, which effectively optimized the membrane structure, enhanced surface hydrophilicity, and regulated charge properties. Consequently, the prepared composite NF membranes integrated high permeability with outstanding dye retention, allowing for efficient removal of dyes from wastewater. A key practical achievement of this strategy is the fabrication of the TFN-0.15 membrane with optimal comprehensive performance: it achieves an 85.6% enhancement in pure water flux compared with the unmodified PA membrane, while maintaining ultrahigh rejection for macromolecular anionic dyes (CR, MeB > 98%) and favorable retention for small-molecule dyes (MeB, MO > 75%) via the synergy of size sieving and electrostatic exclusion, along with excellent long-term operational stability.

In terms of practical implications, the proposed amino-induced *in-situ* bonding strategy provides a scalable and controllable fabrication approach for MOF-modified PA composite NF membranes. Moreover, this strategy is extendable to the modification of other amino-functionalized MOFs and PA-based separation membranes. It offers a novel design concept for developing high-performance membrane materials.

DATA AVAILABILITY

All data generated or analyzed during this study are included in this published article.

CONFLICT OF INTEREST STATEMENT

The authors declare that they have no known competing financial interests or personal relationships that could have appeared to influence the work reported in this paper.

AUTHOR CONTRIBUTIONS

Si Zhang: Data curation; formal analysis; validation; investigation; writing original draft.

Hao Zhang: Data curation; formal analysis; writing review and editing; supervision.

Zhenjie Gu: Methodology; formal analysis; writing review and editing; supervision.

Zhihua Qiao: Conceptualization; formal analysis; writing review and editing; funding acquisition.

ACKNOWLEDGEMENTS

This research was supported by the Science Fund for Distinguished Young Scholars of Tianjin Municipality (no. 23JCJQJC00020).

REFERENCES

[1] Wang Y, Dong Y, Shao J, Zhao Z, Zhai H. Study on Preparation of calcium-based modified coal gangue and its adsorption dye characteristics. Molecules 2024; 29: 2183. https://doi.org/10.3390/molecules29102183

[2] Xia W, Wu Q, Huang R, Tao Y, Wang K, Wu S, Wang S, Wang M, Li Q. Activation of peroxymonosulfate by palygorskite supported Co-Fe for water treatment. RSC Adv 2023; 13: 12483. https://doi.org/10.1039/D2RA07948H

[3] Feng J, Ran X, Wang L, Xiao B, Lei L, Zhu J, Liu Z, Xi X, Feng G, Dai Z, Li R. The synergistic effect of adsorption-photocatalysis for removal of organic pollutants on mesoporous $Cu_2V_2O_7/Cu_3V_2O_8$/g-C_3N_4 heterojunction. Int J Mol Sci 2022; 23: 14264. https://doi.org/10.3390/ijms232214264

[4] Rouhollahi, M; Mohammadi, T; Mohammadi, M; Ahmadzadeh-Tofighy, M. Fabrication of nanocomposite membranes containing Ag/GO nanohybrid for phycocyanin concentration. Sci Rep 2024; 14: 2. https://doi.org/10.1038/s41598-024-73719-8

[5] Zhao DL, Feng F, Shen L, Huang Z, Zhao Q, Lin H, Chung TS. Engineering metal-organic frameworks (MOFs) based thin-film nanocomposite (TFN) membranes for molecular separation. Chem Eng J 2023; 454: 140447. https://doi.org/10.1016/j.cej.2022.140447

[6] Shen L, Cheng R, Yi M, Hung W, Japip S, Tian L, Zhang X, Jiang S, Li S, Wang Y. Polyamide-based membranes with structural homogeneity for ultrafast molecular sieving. Nat Commun 2022; 13: 500. https://doi.org/10.1038/s41467-022-28183-1

[7] Wei S, Chen Y, Hu X, Wang C, Huang X, Liu D, Zhang Y. Monovalent/Divalent salts separation via thin film nanocomposite nanofiltration membrane containing aminated TiO_2 nanoparticles. J Taiwan Inst Chem Eng 2020; 112: 169-179. https://doi.org/10.1016/j.jtice.2020.06.014

[8] Zhang H, Lin B, Pan J, Qi Y, Shen J, Gao C, Van-der-Bruggen B. Carboxyl-functionalized graphene oxide polyamide nanofiltration membrane for desalination of dye solutions containing monovalent salt. J Mem Sci 2017; 539: 128-137. https://doi.org/10.1016/j.memsci.2017.05.075

[9] Aljundi IH. Desalination characteristics of TFN-RO membrane incorporated with ZIF-8 nanoparticles. Desalination 2017; 420: 12-20. https://doi.org/10.1016/j.desal.2017.06.020

[10] Li J, Xie Y, Cheng L, Li X, Liu F, Wang Z. Photo-Fenton reaction derived self-cleaning nanofiltration membrane with MOFs coordinated biopolymers for efficient dye/salt separation. Desalination 2023; 553: 116459. https://doi.org/10.1016/j.desal.2023.116459

[11] Wu X, Yang L, Meng F, Shao W, Liu X, Li M. ZIF-8-incorporated thin-film nanocomposite (TFN) nanofiltration membranes: Importance of particle deposition methods on structure and performance. J Membr Sci 2021; 632: 119356. https://doi.org/10.1016/j.memsci.2021.119356

[12] Wu M, Sun Y, Ji T, Yu K, Liu L, He Y, Yan J, Meng S, Hu W, Fan X, Du D, Liu Y. Fabrication of water-stable MOF-808 membrane for efficient salt/dye separation. J Membr Sci 2023; 686: 122023. https://doi.org/10.1016/j.memsci.2023.122023

[13] Zhang X, Zhang Y, Wang T, Fan Z, Zhang G. A thin film nanocomposite membrane with pre-immobilized UiO-66-NH_2 toward enhanced nanofiltration performance. RSC Adv 2019; 9: 24802. https://doi.org/10.1039/C9RA04714J

[14] Liu L, Huang X, Zhang X, Li K, Ji Y, Yu C, Gao C. Modification of polyamide TFC nanofiltration membrane for improving separation and antifouling properties. RSC Adv 2018; 8: 15102-15110. https://doi.org/10.1039/C8RA01374H

[15] Xiao F, Hu X, Chen Y, Zhang Y. Porous Zr-based metal organic frameworks (Zr-MOFs) incorporated thin-film nanocomposite membrane toward enhanced desalination performance. ACS Appl Mater Interfaces 2019; 11: 47390-47403. https://doi.org/10.1021/acsami.9b17212

[16] Jiang C, Zhang M, Hou Y. Thin-Film Composite Membrane with Porous Interlayer Composed of Dendritic Mesoporous Silica Nanoparticles for Enhanced Nanofiltration. Polymers 2023; 15: 3912. https://doi.org/10.3390/polym15193912

[17] Yu C, Cen X, Ao D, Qiao Z, Zhong C. Preparation of thin-film composite membranes with ultrahigh MOFs loading through polymer-template MOFs induction secondary interfacial polymerization. Appl Surf Sci 2023; 614: 156186. https://doi.org/10.1016/j.apsusc.2022.156186

[18] Plisko T, Burts K, Zolotarev A, Bildyukevich A, Dmitrenko M, Kuzminova A, Ermakov S, Penkova A. Development and investigation of hierarchically structured thin-film nanocomposite membranes from polyamide/chitosan succinate embedded with a metal-organic framework (Fe-BTC) for pervaporation. Membranes 2022; 12: 967. https://doi.org/10.3390/membranes12100967

[19] Song Z, Qiu F, Zaia EW, Wang Z, Kunz M, Guo J, Brady M, Mi B, Urban JJ. Dual-channel, molecular-sieving core/shell ZIF@MOF architectures as engineered fillers in hybrid membranes for highly selective CO_2 separation. Nano Lett 2017; 17: 6752-6758. https://doi.org/10.1021/acs.nanolett.7b02910

[20] Jia Y, Huo X, Gao L, Shao W, Chang N. Controllable design of polyamide composite membrane separation layer structures via metal-organic frameworks: a review. Membranes 2024; 14: 9. https://doi.org/10.3390/membranes14090201

[21] Goh PS, Samavati Z, Ismail AF, Ng BC, Abdullah MS, Hilal N. Modification of liquid separation membranes using multidimensional nanomaterials: revealing the roles of dimension based on classical titanium dioxide. 2023; 13: 448. https://doi.org/10.3390/nano13030448

https://doi.org/10.12974/2311-8717.2026.14.03

© 2026 Zhang *et al.*
This is an open-access article licensed under the terms of the Creative Commons Attribution License (http://creativecommons.org/licenses/by/4.0/), which permits unrestricted use, distribution, and reproduction in any medium, provided the work is properly cited.